ELECTROCHEMISTRY

A self-charging salt water battery for antitumor therapy

Jianhang Huang[1,2†], Peng Yu[1†], Mochou Liao[1], Xiaoli Dong[1], Jie Xu[1], Jiang Ming[1], Duan Bin[1], Yonggang Wang[1], Fan Zhang[1*], Yongyao Xia[1,2*]

Implantable devices on the tumor tissue as a local treatment are able to work in situ, which minimizes systemic toxicities and adverse effects. Here, we demonstrated an implantable self-charging battery that can regulate tumor microenvironment persistently by the well-designed electrode redox reaction. The battery consists of biocompatible polyimide electrode and zinc electrode, which can consume oxygen sustainably during battery discharge/self-charge cycle, thus modulating hypoxia level in tumor microenvironment. The oxygen reduction in battery leads to the formation of reactive oxygen species, showing 100% prevention on tumor formation. Sustainable consumption of oxygen causes adequate intratumoral hypoxic conditions over the course of 14 days, which is helpful for the hypoxia-activated prodrugs (HAPs) to kill tumor cells. The synergistic effect of the battery/HAPs can deliver more than 90% antitumor rate. Using redox reactions in electrochemical battery provides a potential approach for the tumor inhibition and regulation of tumor microenvironment.

INTRODUCTION

Cancer is the leading cause of mortality and disability worldwide, which is characterized by fast growth, easy recurrence, and high metastasis (*1*, *2*). Tremendous efforts have devoted to fight this deadly disease, including classic therapies (surgery, chemotherapy, and radiotherapy) and some burgeoning technologies (such as nanoparticle-based therapy and immunotherapy) (*3*–*7*). However, some limitations still remain on developed anticancer therapies. For example, conventional chemotherapeutic drugs are not specifically targeted to the tumor, which results in systemic toxicity and undesired side effects (*8*–*10*). In addition, immunotherapy usually shows low objective response rate (~20%), as well as some complications including autoimmune diseases, nonspecific inflammation, and unexpected toxicities (*11*–*13*). In contrast, local therapeutic methods, such as implantable devices, have been gaining increasingly high interests because they act directly on tumor tissues, which is able to achieve greater efficacy and minimize systemic side effects (*14*–*16*). Up to now, implantable drug delivery systems are the most investigated implantable devices, which were designed to provide optimal drug release kinetics to improve drug delivery and antitumor efficacy (*17*–*20*). However, the improvement in therapeutic efficacy achieved by the implantable drug delivery systems is limited, especially in the solid tumors, because of the tumor heterogeneity and complex mutual effects between drug molecules and matrix materials during drug release (*21*–*23*). Alternatively, using implantable devices to regulate tumor microenvironment in situ may be a more effective way for cancer therapy.

Metabolism of tumor cells shapes the tumor microenvironment that is different from normal tissues, such as hypoxia and acidic pH (*24*–*27*). Given the key role of tumor microenvironment in the proliferation, invasion, and metastasis of tumors, regulating tumor microenvironment has been considered as a potential avenue to improve therapeutic effect (*28*–*30*). As one of the typical characteristics of solid tumors, hypoxia has been widely investigated (*31*, *32*). On the one hand, it obviously diminishes the therapeutic effectiveness of oxygen-dependent antitumor therapy, such as photodynamic therapy (PDT) and sonodynamic therapy (SDT) (*33*–*35*). On the other hand, hypoxia provides a promising target for precision treatment of tumors, such as hypoxia-activated prodrugs (HAPs) (*36*–*38*). However, HAPs show unsatisfactory efficacy in most phase 3 clinical studies, and one of the main reasons is the uneven and inadequate hypoxia in solid tumors (*39*–*41*). To enhance the hypoxia level of the tumor, injectable nanoparticles as deoxygenation agents (*29*, *39*) and oxygen-consuming PDT (*42*, *43*) or SDT (*44*, *45*) have been reported to scavenge oxygen. However, the retention time of nanoparticles in tumor is usually not more than 2 days, and the short retention time requires deoxygenated agents administrated each time before HAP injection during the whole treatment cycle, which reduces the drug potency and even raises biosafety issues. In addition, the PDT or SDT requires external laser or sound wave, which not only brings high cost and operational complexities but also brings damage on normal tissue when prolonged stimulation of laser or sound wave is applied; once instruments were removed, tumor hypoxia could not be maintained. Therefore, up to now, creating a prolonged hypoxia tumor environment for a course of treatment is still challenging. Here, inspired by the redox reaction of electrode materials in batteries, we designed an implantable self-charging battery to persistently regulate oxygen content, pH, and reactive oxygen species (ROS) in tumor microenvironment.

In this work, the implantable self-charging battery is able to realize persistent oxygen reduction (Fig. 1). As a result, intratumoral oxygen can be consumed steadily and kept to deep hypoxia state [1.9% of intratumoral hemoglobin–bound oxygen saturation (sO_2)] during the treatment period (14 days). In addition, ROS could be produced during the reduction of oxygen in the battery, which showed 100% prevention on tumor formation. For the treatment on solid tumor, tirapazamine (TPZ; a typical drug of HAPs) was used along with the battery, and the synergistic effect between the battery and HAPs showed competitive therapeutic effect (more

[1]Department of Chemistry and Shanghai Key Laboratory of Molecular Catalysis and Innovative Materials, iChEM (Collaborative Innovation Center of Chemistry for Energy Materials), Fudan University, Shanghai 200433, China. [2]Key Laboratory of the Ministry of Education for Advanced Catalysis Materials, College of Chemistry and Materials Science, Zhejiang Normal University, Jinhua 321004, China.
*Corresponding author. Email: zhang_fan@fudan.edu.cn (F.Z.); yyxia@fudan.edu.cn (Y.X.)
† These authors contributed equally to this work.

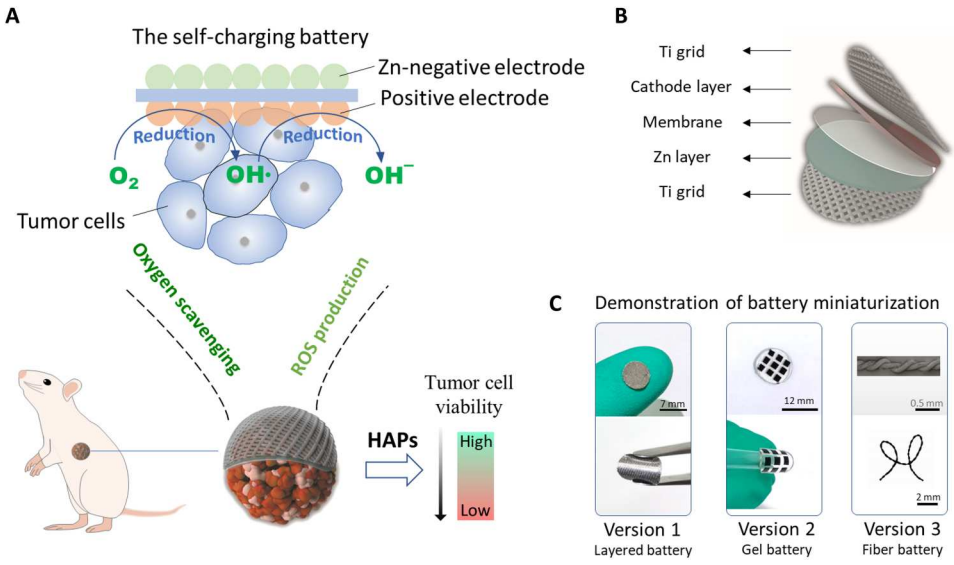

Fig. 1. The rationale of the self-charging battery for tumor therapy. (**A**) Positive electrode material of the battery in the discharging mode is able to effectively reduce the oxygen and results in the production of ROS and hydroxyl ion. With the persistent consumption of oxygen, sustained hypoxia environment can be created, which is able to make full use of HAPs to kill tumor cells. (**B**) Demonstration of structure of the self-charging battery. (**C**) Different battery miniaturization approaches are presented, including layered battery (version 1), gel battery (version 2), and fiber battery (version 3).

than 90% antitumor rate). All the components of the battery are biocompatible and can work well in the physiological environment, which means that no encapsulation for battery is needed and the shape and size of the battery are easy to be manipulated. Some different morphological structures of the self-discharging batteries are shown in Fig. 1C, including layered battery, gel battery, and fiber battery. Considering the spheroid shape of the tumor, the flexible battery could properly cover the tumor. In this work, the layered battery was adopted because of simple preparation process and acceptable flexibility and plasticity, in which the tumor can be wrapped well. Overall, we presented a self-charge battery as a therapeutic device to regulate tumor microenvironment effectively, which rendered a promising platform for antitumor therapy.

RESULTS

Design of the self-charging battery and the oxygen scavenging behavior

The self-charging battery is composed of polyimide (carbonyl compound) as positive material and metallic zinc as negative material, and both of them have high safety and biocompatibility (*46*–*49*). In detail, polyimide material containing carbonyl group synthesized from 1,4,5,8-naphthalenetetracarboxylic dianhydride (*50*) [coded as PNTCDA (fig. S1) for convenience] was selected because of its low redox potential, highly reversibility, and chemical stability. When the battery is discharging, PNTCDA (considered as carbonyl compound, R—C=O) in positive electrode is electrochemically reduced to PNTCDA-H (phenolic compound, R—C—OH) according to Eq. 1. The produced PNTCDA-H have strong reducibility, which can be chemically oxidized back to carbonyl compound by environmental oxygen (Eq. 2). In addition, this chemical charge process is a spontaneous process, which can be considered as a self-charge process. The self-charge process does not destroy the PNTCDA molecule skeleton due to the fact that it only involves the rearrangement of chemical bonds (*51*–*53*), showing high reversibility of electrochemical discharge/chemical charge cycle and fast redox kinetics (Fig. 2A). With the reversible cycle, surrounding oxygen is scavenged as long as the self-charging battery is discharging (in discharging mode).

Electrochemical discharge (electrochemical reduction):

$$2R-C=O\ (\text{carbonyl compound}) + Zn + 2H_2O \rightarrow 2R-C-OH\ (\text{phenolic compound}) + Zn^{2+} + 2OH^- \quad (1)$$

Self-charge (chemical charge or chemical oxidation):

$$4R-C-OH\ (\text{phenolic compound}) + O_2 \rightarrow 4R-C=O\ (\text{carbonyl compound}) + 2H_2O \quad (2)$$

To prove the above redox mechanism, the electrochemical performance of PNTCDA was firstly investigated in 1 M $ZnSO_4$ electrolyte. There are two pairs of redox peaks (−0.53/−0.62 V and −0.27/−0.45 V versus Ag/AgCl, respectively) in cyclic voltammetry (CV) curves (Fig. 2B), showing high reversibility and fast kinetics during redox (figs. S2 and S3). Further characterizations demonstrated that the electrochemical redox of PNTCDA is based on the storage/release of proton (H^+) and refers to a little Zn^{2+} storage/release in $ZnSO_4$ electrolyte (figs. S4 to S8). The discharge product of PNTCDA (i.e. PNTCDA-H) with low redox potential was easy to be reoxidized to PNTCDA by surrounding oxygen, and the corresponding open circuit voltage (OCV) of PNTCDA‖Zn battery took about 10 hours to recover to 1.1 V (Fig. 2C and fig. S9). Furthermore, the self-charge process under different atmospheres and the stability of electrochemical discharge/self-charge cycle in 1 M $ZnSO_4$ electrolyte can be found in figs. S10 to S15.

Second, as an implantable device, the oxygen scavenging performances of PNTCDA‖Zn battery in biocompatible electrolyte, i.e.,

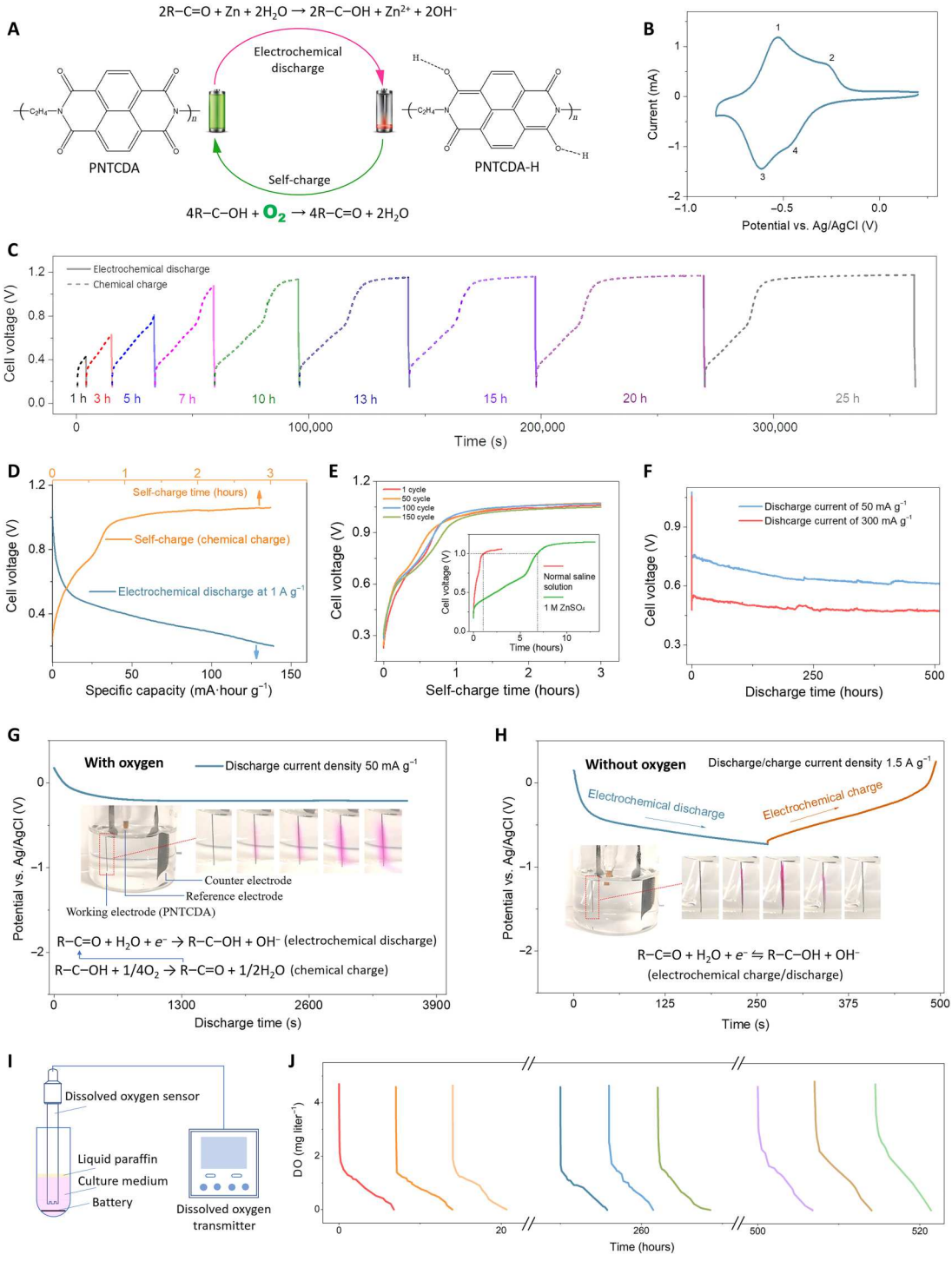

Fig. 2. Redox mechanism and characterizations of oxygen scavenging behavior. (**A**) Demonstration of the electrochemical discharge/self-charge cycle. (**B**) CV of PNTCDA in 1 M $ZnSO_4$ electrolyte at scan rates of 1 mV s^{-1}. Counter electrode is Zn foil, and reference electrode is Ag/AgCl. (**C**) Chemical charge (with different self-charge times) and electrochemical discharge curves (discharge current density of 1 A g^{-1}) of PNTCDA‖Zn battery as function of time. The battery contains PNTCDA-positive electrode, Zn-negative electrode, and 1 M $ZnSO_4$ electrolyte. (**D**) Electrochemical discharge curve (discharge current density of 1 A g^{-1}) and self-charge curve of PNTCDA‖Zn battery in biocompatible normal saline solution under air atmosphere. (**E**) Comparison of chemical charge (self-charge) curves after different electrochemical discharge/chemical charge cycles. Inset: Comparison of chemical charging behavior of PNTCDA in normal saline electrolyte and $ZnSO_4$ electrolyte. (**F**) Discharge curves of PNTCDA‖Zn battery in normal saline electrolyte under air atmosphere at current densities of 50 mA g^{-1} (blue curve) and 300 mA g^{-1} (red curve) as a function of discharge time. (**G**) Visual oxygen scavenging of PNTCDA electrode at 50 mA g^{-1} under air atmosphere enabled by pH indicator (phenolphthalein). (**H**) Color change of electrolyte during electrochemical discharge/charge at 1.5 A g^{-1} under Ar atmosphere. Working electrode, PNTCDA; counter electrode, activated carbon; reference electrode, Ag/AgCl. (**I**) Equipment for online monitoring on dissolved oxygen in nutrient solution. (**J**) Change tendency of dissolved oxygen content.

normal saline solution, was further demonstrated. The electrochemical discharge/self-charge profile of PNTCDA‖Zn battery in normal saline electrolyte under air atmosphere was shown in Fig. 2D. The chemical charge rate of PNTCDA electrode in normal saline electrolyte was much higher than that in $ZnSO_4$ electrolyte. It only took 66 min to reach an OCV of 1.0 V under air atmosphere, much faster than that (~6 hours) in $ZnSO_4$ electrolyte (inset of Fig. 2E). Furthermore, the battery in normal saline showed more stable chemical charge performance (Fig. 2E) than that in $ZnSO_4$ electrolyte (fig. S15). The OCV of battery after long cycles (150 cycles) could be restored as fast as the fresh battery does in normal saline (Fig. 2E), and the corresponding cycle performance was shown in fig. S16. This obvious difference on self-charging performance could be explained by the different stabilities of carbonyl compound after storing different ions (*54*–*56*), i.e., storage of H^+ and Na^+ in normal saline solution and that of H^+ and Zn^{2+} in $ZnSO_4$ electrolyte. In addition, the self-charge process will take place as long as the battery is discharging. Thus, the electrochemical discharge/self-charge cycle will reach an equilibrium when the self-charge rate is equal to the electrochemical discharge rate, resulting in a stable discharge voltage (Fig. 2F), which can be considered as a proof for the sustainable consumption of oxygen.

Oxygen scavenging could be further demonstrated by the pH increase in electrolyte, because when the discharge product of PNTCDA was oxidized by oxygen, oxygen itself will be reduced to hydroxyl. Thus, phenolphthalein was used to visualize pH change. As expected, with the continuous battery discharge, the color of phenolphthalein around PNTCDA electrode gradually turned to red (Fig. 2G, movie S1, and fig. S17), indicating the reduction of oxygen. Furthermore, the visualization strategy can be used as a simple in situ method to investigate proton storage behavior of electrode materials. Figure 2H (movie S2) monitored the color change of electrolyte when the PNTCDA electrode was electrochemically charged/discharged under argon atmosphere in normal saline electrolyte (argon atmosphere is used to eliminate the interference of dissolved oxygen). It can be seen that the electrolyte around electrode turned red during electrochemical discharge and turned back to the transparent during electrochemical charge, demonstrating that reversible proton storage/release was involved during electrochemical redox of PNTCDA in normal saline electrolyte. To further demonstrate the oxygen scavenging behavior, direct monitoring on dissolved oxygen content was conducted (Fig. 2I). In addition, short-circuited battery was used in this test to keep the battery in discharging mode, thus making full use of self-charge behavior for consuming oxygen. The short-circuited battery was put into a tube filled with 15 ml of culture medium to simulate physiological environment, which was sealed with liquid paraffin to insulate the outside air. As can be seen in Fig. 2J, only 5 to 7 hours is needed for the battery to deplete dissolved oxygen in electrolyte. Furthermore, after continuous work for more than 500 hours and multiple cycles, the battery still maintained a steady oxygen consumption efficiency, which strongly proofs its long-term and stable oxygen scavenging behavior.

Performance of the battery in modulating tumor microenvironment

Tumor microenvironment is considered as the "soil" that tumor relies to grow. In addition, regulation on the tumor microenvironment shows great potential on suppressing tumor growth. Given the strong ability on oxygen scavenging, the self-charging battery provides an effective platform to regulate tumor microenvironment for directly displaying therapeutic effect and enhancing the potency of HAPs [which shows cytotoxicity only under hypoxic environment (*37*)] (Fig. 3A).

The change of intracellular O_2 level in 4T1 cells after induction of battery was firstly measured using $[Ru(dpp)_3]Cl_2$, whose red fluorescence intensity is proportional to the hypoxic degree (*57*). Compared with the control group, there was negligible difference of red fluorescence intensity in TPZ or battery in circuit break mode [unworking battery (UB)] group. In contrast, after 4T1 cells coincubated with the battery in discharging mode [discharging battery (DB)], there was a twofold intracellular red fluorescence intensity higher than that in control group, suggesting the strong oxygen consumption ability of DB (Fig. 3, B and F). Thereafter, we investigated the synergic effect of DB with TPZ for treating 4T1 cells. Cell Counting Kit-8 (CCK-8) results showed that cell viability was comparable in control, TPZ, and UB groups, indicating that TPZ alone is futile under inadequate hypoxic condition. In contrast, 98% of 4T1 cells was essentially killed by DB + TPZ treatment (Fig. 3G and fig. S18). Cytotoxicity of different treatments was also verified by the fluorescence imaging of calcein acetoxymethyl ester (calcein-AM) (staining living cells with green fluorescence) and propidium iodide (PI) (staining dead cells with red fluorescence). Almost all 4T1 cells were stained with red fluorescence in DB + TPZ group, implying its strongest antitumor effect compared with other groups (Fig. 3C), which demonstrate that the severe hypoxic environment created by DB can make full use of TPZ. Furthermore, the change of pH in 4T1 cells with different treatments was detected using intracellular pH probe [2′,7′-bis(2-carboxyethyl)-5(6)-carboxyfluorescein (BCECF-AM)] (*58*). In DB-treated 4T1 cells, increased pH in culture medium was observed (Fig. 3, D and H, and fig. S19). There is about threefold green fluorescence intensity of BCECF stronger than that in control group. It can be ascribed to the hydroxyl ions derived from reduction of oxygen, which is consistent with the result in Fig. 2G. Notably, cell viability in DB-alone group decreased to 18% (Fig. 3G), indicating that DB itself can exert antitumor effect to a certain extent. This result can be explained by the production of ROS during reduction of oxygen induced by DB, which kill cancer cells effectively (*59*–*61*). To verify this point, ROS probe, 2,7-dichlorodihydrofluorescein diacetate (DCFH-DA), was used to detect the production of ROS. About sixfold green fluorescence of DCFH-DA brighter than that in control group was shown in DB group (Fig. 3, E and I), indicating that DB can efficiently produce ROS after the incubation with 4T1 cells. The production of ROS is also proved by terephthalic acid (TA) as a fluorescence probe (fig. S20). In conclusion, this self-charging battery has great potential to be used as a multifunctional platform to produce ROS and persistent scavenge oxygen to make full use of HAPs for antitumor therapy.

Improved cancer therapeutic efficacy by synergistic effect of battery and HAPs

On the basis of the effective and permanent regulation on tumor microenvironment by the self-charging battery, in vivo antitumor studies of the self-charging battery were conducted (schematic illustration of the battery implantation process was provided in fig. S21). In addition, the ability of DB to create a long-term hypoxic

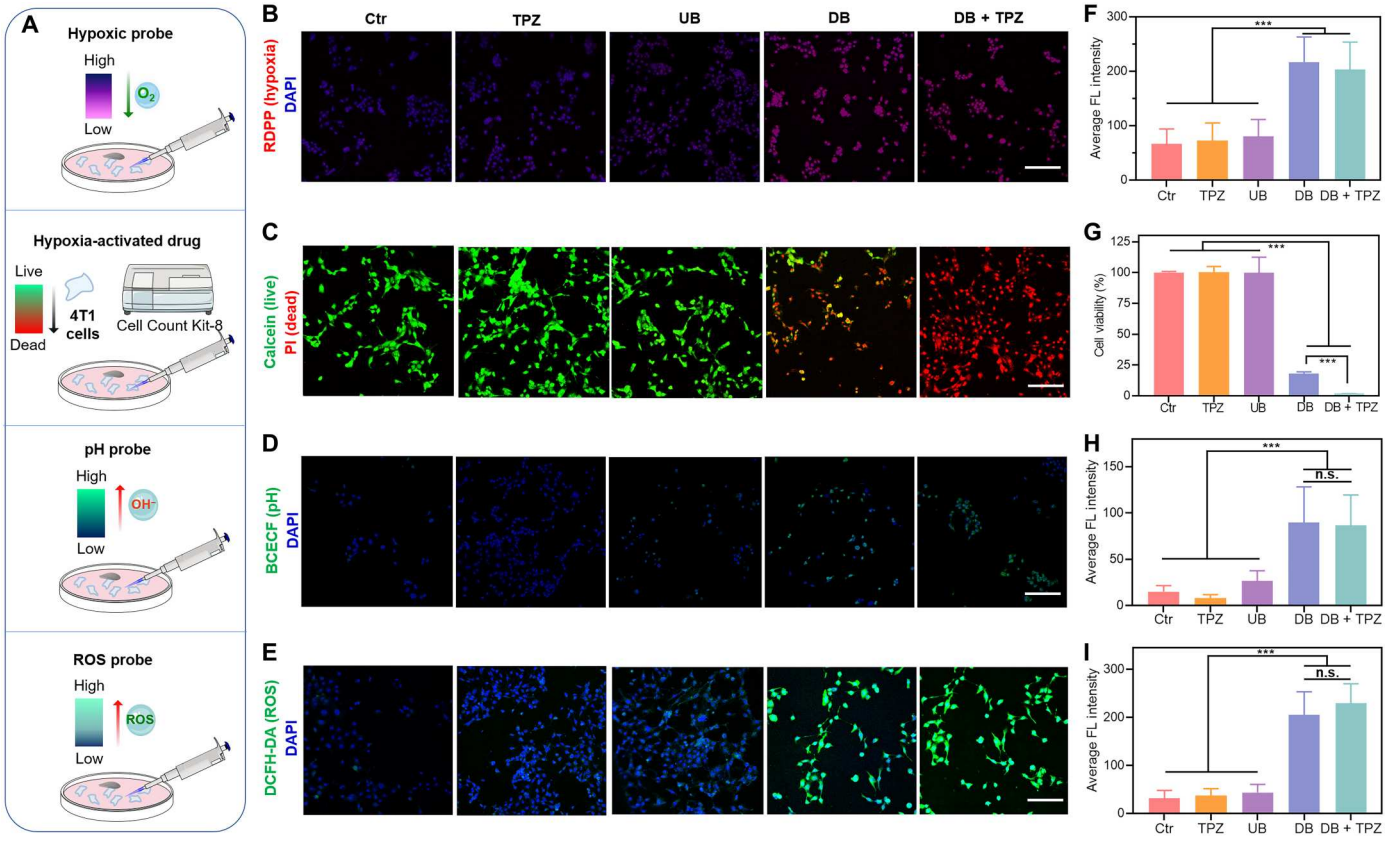

Fig. 3. The self-charging battery regulated the tumor microenvironment in vitro. (**A**) Schematic illustration of the regulating tumor microenvironment experiments in vitro using self-charging battery. (**B**) Fluorescence images of intracellular hypoxic condition. (**C**) Live and dead staining images of 4T1 cells treated with five groups. (**D**) Fluorescence images of intracellular pH change. (**E**) Fluorescence images of intracellular ROS production. (**F**) The corresponding quantitative fluorescence (FL) intensity for (B). (**G**) Relative cell viability of 4T1 cells with different treatments (n = 3). (**H**) The corresponding quantitative fluorescence intensity for (D). (**I**) The corresponding quantitative fluorescence intensity for (E). Ctr, control; RDPP, $[Ru(dpp)_3]Cl_2$; n.s., not significant. ***P < 0.001. Scale bars, 200 μm.

environment within subcutaneous 4T1 tumor for HAPs treatment was explored (Fig. 4, A to J). First, average intratumoral hemoglobin–bound sO_2 was measured after the tumor treated with implanted battery or intravenous injection of saline. To avoid the influence of different mice to make the results credible, the experiment was carried out on one mouse with a tumor on the left and right of the mouse legs, respectively (Fig. 4E). Intratumoral hemoglobin–bound sO_2 in battery-treated tumor was reduced constantly from day 1 to day 14 and decreased to 1.9% on day 14, which was significantly lower than that of 14.1% in control group (tumor treated with saline) on day 14 (Fig. 4, E and F). Furthermore, tumor hypoxia level was detected by classical immunofluorescent staining of hypoxia-inducible factor-1α (HIF-1α), whose green fluorescence intensity is proportional to the hypoxic degree. On day 1, compared with the control group, there was no obvious difference of fluorescence intensity in TPZ and UB groups, whereas about fourfold intensity of the green immunofluorescence was shown in DB and DB + TPZ group (Fig. 4B and fig. S22). On days 7 and 14, almost saturated green fluorescence appeared in DB group, indicating that the long-term and deep intratumoral hypoxia can be created by DB (Fig. 4, G and H). To explore the hypoxia levels at different depths of the tumor, tumors were longitudinally evenly divided into five slices and then stained with anti–HIF-1α immunofluorescent (red) antibody to probe the hypoxic condition (fig. S23). The relative HIF-1α–positive area in battery-treated tumor showed a 4.5- to 34.5-fold higher than that of the tumor in control group, indicating that the battery could create the hypoxic condition at various depths of the tumor. Furthermore, ROS induced by the self-charging battery was also detected in the in vivo experiment (Fig. 4C and fig. S24), which was consistent with the result in vitro (Fig. 3E). The produced ROS was able to suppress tumor growth, and the tumor volume shrank to 26% (Fig. 4I, blue curve). In addition, biofouling effect on the battery was investigated, which showed that the battery kept the ability to continuously consume oxygen although biofouling on battery leads to slower rate of oxygen consumption with longer implantation time (figs. S25 to S27). Note that the implanted battery could not be degraded in vivo, and it was taken out and then characterized after tumor treatment (fig. S28). X-ray diffraction (XRD) results showed that little amount of zinc chlorate hydrate was detected on zinc electrode (fig. S28A). However, the small amount of zinc chlorate hydrate showed no obvious influence on electrochemical performance of zinc electrode (fig. S28D). On the other hand, obvious decay on electrochemical performance of PNTCDA electrode was observed (fig. S28C), which can be ascribed to the biofouling effect and deterioration of positive electrode materials.

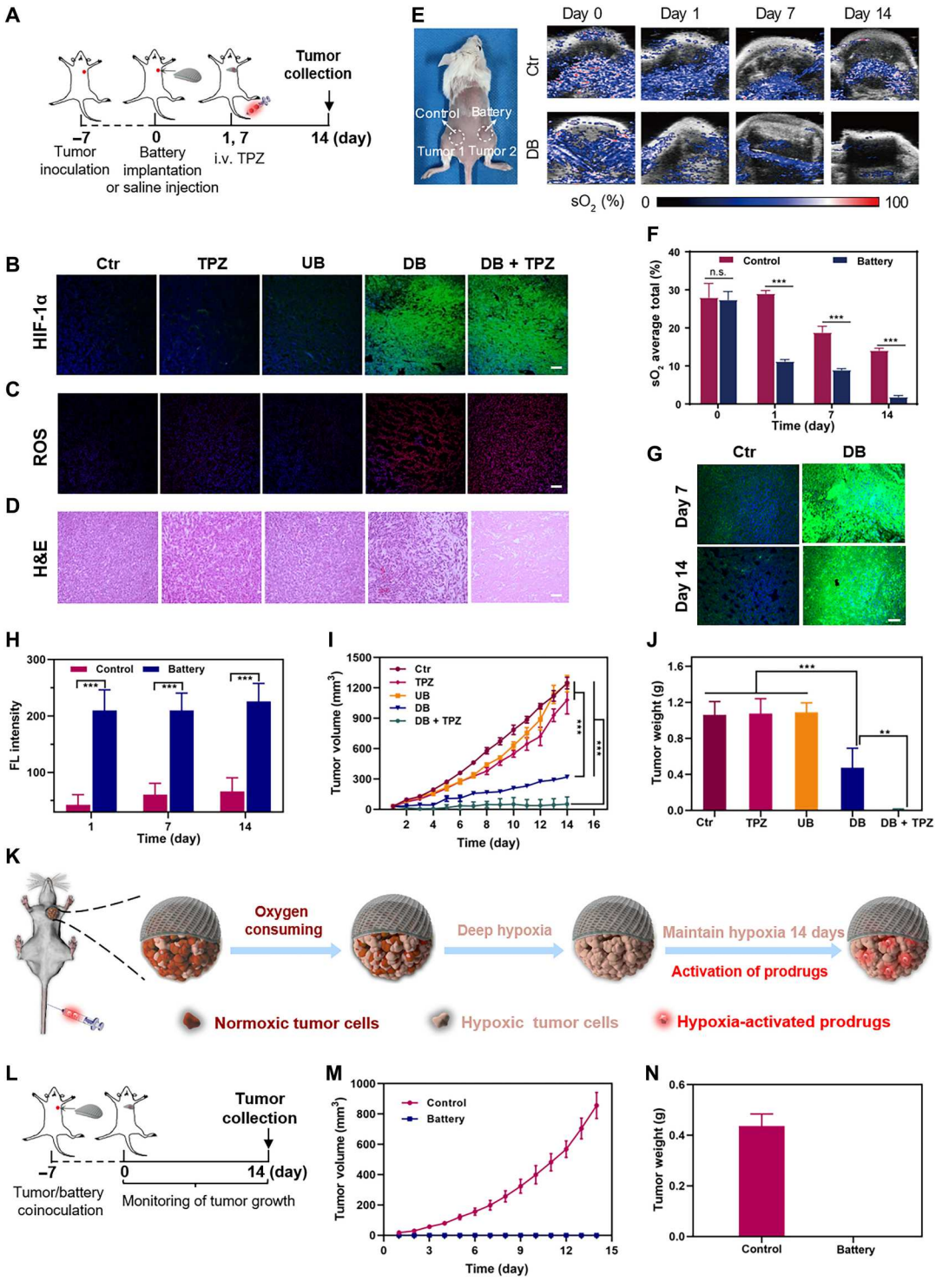

Fig. 4. The self-charging battery enhances antitumor therapy by maintaining tumor hypoxia for whole treatment cycle. (**A**) Schematic diagram of the treatment process of self-charging battery in inhibition of tumor growth study. TPZ was intravenously (i.v.) injected on days 1 and 7 if necessary at a dose of 20 mg kg^{-1}. (**B**) Immunofluorescence staining images of HIF-1α in various groups on day 1. Scale bar, 100 μm. (**C**) ROS staining images of tumor tissues collected from mice 24 hours after different treatments. Scale bar, 100 μm. (**D**) H&E staining images of tumor tissues collected from mice 24 hours after different treatments. Scale bar, 200 μm. (**E** and **F**) Photoacoustic imaging (E) and quantitative results of intratumoral hemoglobin–bound sO_2 (F) in control and battery groups. (**G** and **H**) HIF-1α staining images (G) and corresponding fluorescence intensity (H) in control and battery groups on days 7 and 14, respectively. Scale bar, 100μm. (**I**) Variation of tumor volume after different treatments (n = 5). (**J**) Average tumor weight on day 14 in five groups (n = 5). (**K**) Schematic diagram of the synergic effect between the self-charging battery and HAPs. (**L**) Schematic diagram of the treatment process in prevention of tumor formation. (**M**) Daily curve of tumor volume of mice in control (saline) and battery groups (n = 6). (**N**) Average tumor weight of mice on day 14 in two groups (n = 6). ***P < 0.001 and **P < 0.01.

Next, the synergic effect between the self-charging battery and HAPs for cancer therapy was evaluated in vivo. Compared with control group (intravenous injection of saline), tumor growth was not restricted by TPZ or UB alone but significantly inhibited by DB + TPZ treatment. On day 14, tumor disappeared in 80% of the mice (n = 5), and the average tumor volume was reduced by 90% in DB + TPZ group (Fig. 4I). In addition, the average tumor weight in DB + TPZ group decreased to 10% of that in control group (Fig. 4J). The excised tumors on day 14 were weighted and photographed (fig. S29). Moreover, hematoxylin and eosin (H&E) staining assays further confirmed the prominent tumor apoptosis after DB + TPZ treatment (Fig. 4D). To investigate the effective depth of hypoxia-driven treatment, tumor cell viability was performed on the tumor after treatment with DB + TPZ (fig. S30).

The tumors were longitudinally evenly divided into five slices and then stained with H&E to probe tumor cell viability. Results showed tumor cells were obviously killed by the DB + TPZ treatment at various depths compared with control group. These results suggest that preadministration of DB to create a long-term hypoxic environment can greatly enhance the antitumor efficacy of TPZ. In addition, no obvious changes of body weight and histological morphology of mice major organs were observed (figs. S31 and S32), indicating that the battery and the combined therapy have few side effects in vivo. The few side effects resulted from the different reactions on positive and negative electrodes of battery. As illustrated in the Fig. 1A, oxygen was reduced and ROS was produced in the PNTCDA-positive electrode. Zinc electrode only revolved in the production of zinc ions (figs. S33 and S34). When the battery was implanted in vivo, the PNTCDA-positive electrode was attached to the tumor, and the zinc electrode was attached to the skin, which focuses the hypoxia and ROS region on the tumor. To investigate the side effect of battery to the normal tissues, the hypoxic condition, ROS level, and cell viability in normal tissue (skin) on the side of zinc electrode after the treatment of the battery were then measured. Results showed no obvious side effect to the normal tissues in vivo (figs. S35 to S38). In addition, on the basis of the produced ROS of DB, the potential of DB in preventing tumorigenesis was explored (Fig. 4, L to N). Tumor volume increased continuously in control group, while it was maintained zero in DB group (Fig. 4M). No tumor mass survived in DB group on day 14 (Fig. 4N and fig. S39), which verifies the notable tumorigenesis suppression effect of DB. Meanwhile, mice body weight remained stable during the treatment period (fig. S40A), and H&E staining results of mice with battery implantation showed no obvious side effects to the skin (fig. S40, B and C), suggesting the good biocompatibility of DB.

DISCUSSION

In summary, we have designed an implantable aqueous self-charging PNTCDA‖Zn battery that can create tumorous hypoxic environment to activate hypoxia-based antitumor therapy. Compared with other methods to create hypoxic environment, the most advantage of the implantable battery is the ability to maintain continuous tumor hypoxic environment for a long time (a course of treatment, 14 days) by one-time implantation. The hypoxia created by the previous methods, such as deoxygenation agents and oxygen-consuming PDT and SDT, is intermittent. The short retention time of deoxygenation agents requires repeated administration, continuous stimulation of PDT and SDT brings damage to the normal tissue, and above disadvantages reduce drug potency and even raise biosafety issues. In this work, oxygen can be persistently consumed during the reversible electrochemical discharge/self-charge cycle of polyimide electrode material of battery and can maintain tumor hypoxic environment for at least 14 days in vivo. Meanwhile, competitive therapeutic effect was achieved after combined treatment of battery with TPZ. Tumor disappeared in 80% of the mice, and the average tumor volume was reduced by 90% in a 4T1 tumor model. In addition, the battery exerted a 100% prevention of tumorigenesis based on the production of ROS during oxygen reduction in battery. Furthermore, the battery components are biocompatible, which minimized the harm of battery implantation. Moreover, there are abundant redox chemistry that can be used in battery systems, which provide great potential to develop other therapeutic devices, such as electrochemiluminescence, wearable device, interventional therapy, inflammatory microenvironment regulation, and electric nerve stimulation.

MATERIALS AND METHODS

Materials

1,4,5,8-naphthalenetetracarboxylic dianhydride (NTCDA), ethylene diamine (EDA), *N*-methylpyrrolidone (NMP), $ZnSO_4{\cdot}7H_2O$, NaCl, zinc powder, 1% phenolphthalein solution, and TA were obtained from Sinopharm Chemical Reagent Co. Ltd. 4T1 cells were provided by American Type Culture Collection (USA). RPMI 1640 medium was provided by Gibco, Thermo Fisher Scientific, USA.

Characterization

Fourier transform infrared spectroscopy (FTIR) spectrum was recorded with a NICOLET 6700 FTIR Spectrometer using KBr pellets. XRD patterns were collected on a x-ray diffractometer (Bruker D8 Advance, Germany) with Cu Kα radiation (λ = 0.15406 nm). Scanning electron microscopy images were obtained on field-emission JEOL JSM-6390 microscope. Transmission electron microscopy and energy-dispersive x-ray spectrometry mapping were performed on JEOL JEM-2010 microscope. The ultraviolet (UV) absorbance at 450 nm was measured using a multireader (TECAN, Infinite M200, Germany). The emission of TA was detected by Edinburgh Instruments FLS980 spectrometer.

Material preparation

PNTCDA was prepared according to previous works (*50*). In a typical synthesis, equimolar NTCDA and EDA were added into the solvent of NMP. The mixture solution was refluxed for 6 hours. The obtained product was filtrated, washed several times with ethanol and NMP, vacuum-dried at 120°C for 12 hours, and then heated in nitrogen atmosphere for 8 hours at 300°C.

Electrochemical measurements

Electrochemical measurements were performed with CR2016 cointype cells or flooded cells. All the self-charging performances were conducted with flooded cells unless otherwise stated. For coin cell used for galvanostatic charge/discharge test with $ZnSO_4$ electrolyte, PNTCDA served as positive electrode, and zinc metal foil as negative electrode, a glass fiber as separator, and aqueous 1 M $ZnSO_4$ as electrolyte. For flooded cells used in self-charging performances, PNTCDA was used as positive electrode, zinc metal foil was used as negative electrode, and aqueous 1 M $ZnSO_4$ or normal saline solution was used as electrolyte. For the in situ visualization of deoxygenation test, two drops of 1% phenolphthalein solution were added into electrolyte, and active carbon electrode and Ag/AgCl electrode were used as counter electrode and reference electrode, respectively. The working electrode was fabricated by compressing a mixture of the active materials of PNTCDA, the conductive material [Ketjenblack (KB)], and the binder [polytetrafluoroethylene (PTFE)] in a weight ratio of active materials/KB/PTFE = 6:3:1 onto a Ti grid at 25 MPa, the areal loading density is about 2.0 mg cm^{-2}. Active carbon counter electrode was fabricated by compressing a mixture of the active carbon, the conductive material (acetylene black), and the binder (PTFE) in a weight ratio of active carbon/acetylene black/PTFE = 8:1:1 onto a Ti grid at 25

MPa. Galvanostatical discharge/charge performances and galvanostatical discharge/chemical charge performances were conducted on a battery test system (Neware BTS 4000) or electrochemical workstation (BioLogic VSP-300). Cyclic voltammograms were carried out using BioLogic VSP-300.

Calculation of redox potential based on Nernst equation

Electrode reaction:

$$\mathrm{PNTCDA} + 2\ \mathrm{H^+} + 2e^- \rightleftharpoons \mathrm{H_2PNTCDA} \quad (3)$$

Nernst equation:

$$\varphi = \varphi^\theta + \frac{2.303\ RT}{nF} lg \frac{[\mathrm{PNTCDA}][H^+]^2}{[\mathrm{H_2PNTCDA}]}\varphi^\theta + \frac{0.0592}{n} lg \frac{[\mathrm{PNTCDA}][H^+]^2}{[\mathrm{H_2PNTCDA}]} \quad (4)$$

where ϕ is the electrode potential, ϕ^θ is the standard potential, R is the universe gas constant of 8.314 J K^{-1} mol^{-1}, T is the temperature of 298.15 K, n is the electron transfer numbers, and F is the Faraday constant of 96,500 C mol^{-1}. The activity of solid PNTCDA and H_2PNTCDA is considered as 1, and n is 2; the equation can be further simplified as follow:

$$\varphi = \varphi^\theta + \frac{0.0592}{2} lg[\mathrm{H^+}]^2 = \varphi^\theta + 0.0592[\mathrm{H^+}] \quad (5)$$

from which the potential difference of PNTCDA in a 0.3 M H_2SO_4 solution and in 1 M $ZnSO_4$ aqueous electrolyte (pH 5) can be calculated as follow:

$$\Delta\varphi = 0.592\ lg\ \frac{[\mathrm{H^+}]_1}{[\mathrm{H_+}]}\mathrm{V} = 0.0592\ lg\ \frac{0.6}{10^{-5}}\mathrm{V} = 0.26\ \mathrm{V} \quad (6)$$

Monitoring of dissolved oxygen in cell culture medium

Dissolved oxygen content was monitored by dissolved oxygen meter. Specifically, a self-charging battery was put into a test tube filled with 15 ml of culture medium, which was then sealed with liquid paraffin to insulate the outside air. The distance between oxygen electrode and the battery was fixed at 3 mm. When the content of dissolved oxygen decreased to zero, the battery was moved to another fresh culture medium for the next test.

Cell viability

4T1 cells were cultured in RPMI 1640 medium containing 10% fetal bovine serum and 1% penicillin/streptomycin at 37°C with 5% CO_2 atmosphere. For in vitro cell cytotoxicity test, 4T1 cells were seeded in a 24-well plate at a density of 2×10^4 cells per well and cultured for 24 hours. Then, medium was replaced with fresh medium, TPZ (7.5 μg ml^{-1}), UB, DB, or DB + TPZ (7.5 μg mL^{-1}) was added, respectively. After further co-incubation for 24 hours, a solution consisted of 100 μl of CCK-8 and 900 μl of fresh RPMI 1640 medium was added. After 1 hour, the UV absorbance at 450 nm was measured. Cell viability was calculated by following formula: cell viability (%) = (mean absorbance value of treatment group − mean absorbance value of blank group / mean absorbance value of control group − mean absorbance value of blank group) × 100%.

Calcein-AM/PI stain assay

To evaluate antitumor efficacy in vitro, 4T1 cells were seeded in a 24-well plate. After adherence to the hole, cells were coincubated with various samples for 2 hours, followed by calcein-AM/PI staining for 25 min. Next, cells were washed three times with 1× phosphate-buffered saline (PBS) and then fixed with 4% paraformaldehyde before imaging using confocal laser scanning microscope. Excitation and emission are described as follows: calcein-AM, E_x = 488 nm and E_m = 500 to 540 nm; PI, E_x = 561 nm and E_m = 570 to 670 nm.

Intracellular pH detection and hypoxia evaluation

To measure intracellular pH, 4T1 cells were seeded in a six-well plate for 24 hours and then replaced with fresh medium containing 5 μM BCECF-AM for 1-hour staining. Next, free BCECF-AM was washed with 1× PBS, and then fresh medium, TPZ (7.5 μg ml^{-1}), UB, DB, and DB + TPZ (7.5 μg ml^{-1}) was added, respectively, followed by coincubation for 2 hours. After washing three times with 1× PBS, cells were fixed with 4% paraformaldehyde for 15 min. The cell nuclei were stained with 4′,6-diamidino-2-phenylindole-dihydrochloride (DAPI) for another 15 min at room temperature, followed by washing three times with 1× PBS. Last, BCECF-AM fluorescence intensity was detected by confocal laser scanning microscope (E_x = 488 nm and E_m = 530 nm).

For intracellular hypoxia evaluation, the method is similar to the above except that 5 μM BCECF-AM was replaced with 5 μM $[Ru(dpp)_3]Cl_2$ and the staining time was extended to 4 hours. Then, fluorescence imaging was carried out using confocal laser scanning microscope (E_x = 513 nm and E_m = 600 to 700 nm).

Intracellular ROS assessment

To assess the intracellular ROS production, DCFH-DA staining assay was used. Briefly, 4T1 cells preseeded in a 24-well plate were stained with DCFH-DA (10 μM) for 30 min at 37°C. After washing with 1× PBS, fresh medium, TPZ (7.5 μg ml^{-1}), UB, DB, and DB + TPZ (7.5 μg ml^{-1}) was incubated with cells for 2 hours, respectively. Then, those 4T1 cells were fixed with 4% paraformaldehyde and stained nuclei with DAPI for 15 min. Last, the fluorescent emission of DCFH-DA was detected using confocal laser scanning microscope (E_x = 488 nm and E_m = 530 nm). The relative fluorescence intensity of the above images was calculated by ImageJ software.

Cell medium pH detection

4T1 cells were seeded in a six-well plate and incubated for 24 hours. Then, the medium was changed with fresh RPMI 1640 medium, and cells were treated with above five treatments. Culture medium was taken out at 10, 20, 30, 60, and 120 min, respectively, whose pH was detected by a pH detector.

Ethical statement

All animal experiments were in agreement with the guidelines of the Institutional Animal Care and Use Committee of Fudan University and permitted by the Shanghai Science and Technology Committee.

Inhibition of tumorigenesis study

Female Balb/c mice (15 to 20 g) were provided by Shanghai SLAC Laboratory Animal Co. Ltd. Mice were inoculated subcutaneously with 1×10^6 4T1 cells per mouse in the right armpit and then randomly divided into two groups: control group and battery group

($n = 6$). For battery group, battery was implanted immediately after 4T1 cells inoculation. It was regarded as day 1 when tumor volume in the control group reached to about 40 mm^3. Tumor growth and body weight of each mouse were monitored until day 14. The diameter of tumors was measured with a digital caliper, and the volume was calculated by the following equation: $V\ (mm^3) = (W^2 \times L)/2$, where W (width) is the shorter diameter and L (length) is the longer diameter perpendicular to W.

Suppression of tumor growth study

Female Balb/c mice (15 to 20 g) were inoculated subcutaneously with 1×10^6 4T1 cells per mouse in the right armpit. Once the tumor volume reached to ~40 mm^3, mice were randomly divided into five groups: control, TPZ, UB, DB, and DB + TPZ ($n = 5$). On day 1, TPZ was intravenously injected if necessary at a dose of 20 mg kg^{-1}. Tumor volume and mice body weight were measured every day until day 14. Representative mice of each group were photographed on days 4, 7, and 14. On day 14, mice were all euthanized, and then tumors were excised, weighed, and photographed.

Mice organ H&E, tumor H&E, ROS, and HIF-1α staining

When tumor volume increased to ~150 mm^3, mice were treated with different treatments. For histology analysis, tumors and normal organs including the heart, liver, spleen, lung, and kidney were harvested 24 hours after treatments, fixed with 4% paraformaldehyde for 1 day, and then sectioned at a thickness of 10 to 20 μm. Tissue slices were stained with H&E before examination using inverted fluorescence microscope.

To evaluate the hypoxic conditions in the tumors after different treatments, HIF-1α staining was conducted using anti–HIF-1α antibody (diluted with 1:200; ab113642). Images was captured by confocal laser scanning microscope. The hypoxic degree was evaluated by the green fluorescence intensity of anti–HIF-1α antibody using ImageJ software.

To assess ROS production in tumor tissues, dihydroethidium probe was used. Images was captured by confocal laser scanning microscope (E_x = 488 nm and E_m = 590 to 610 nm). Specific red fluorescence intensity was calculated by ImageJ software.

Photoacoustic imaging in vivo

The tumor sO_2 was evaluated by VisualSonics LAZR and Vevo 2100 Photoacoustic CT Scanner. Total hemoglobin and oxygenated hemoglobin were measured at the wavelength of 850 and 750 nm after battery implantation. The sO_2 was the percentage of oxygenated hemoglobin in the total hemoglobin.

Supplementary Materials

This PDF file includes:
Figs. S1 to S40
Legends for movies S1 and S2

Other Supplementary Material for this manuscript includes the following:
Movies S1 and S2

REFERENCES AND NOTES

1. R. L. Siegel, K. D. Miller, H. E. Fuchs, A. Jemal, Cancer statistics, 2021. *CA Cancer J. Clin.* **71**, 7–33 (2021).
2. F. Bray, M. Laversanne, E. Weiderpass, I. Soerjomataram, The ever-increasing importance of cancer as a leading cause of premature death worldwide. *Cancer* **127**, 3029–3030 (2021).
3. J. Wang, Y. Y. Li, G. J. Nie, Multifunctional biomolecule nanostructures for cancer therapy. *Nat. Rev. Mater.* **6**, 766–783 (2021).
4. M. Kenchegowda, M. Rahamathulla, U. Hani, M. Y. Begum, S. Guruswamy, R. A. M. Osmani, M. P. Gowrav, S. Alshehri, M. M. Ghoneim, A. Alshlowi, D. V. Gowda, Smart nanocarriers as an emerging platform for cancer therapy: A review. *Molecules* **27**, 146 (2022).
5. Q. He, J. J. A. M. Shi, MSN anti-cancer nanomedicines: Chemotherapy enhancement, overcoming of drug resistance, and metastasis inhibition. *Adv. Mater.* **26**, 391–411 (2014).
6. V. M. Konala, S. Adapa, W. S. Aronow, Immunotherapy in bladder cancer. *Am. J. Ther.* **29**, E334–E337 (2022).
7. J. M. Llovet, F. Castet, M. Heikenwalder, M. K. Maini, V. Mazzaferro, D. J. Pinato, E. Pikarsky, A. X. Zhu, R. S. Finn, Immunotherapies for hepatocellular carcinoma. *Nat. Rev. Clin. Oncol.* **19**, 151–172 (2022).
8. V. Schirrmacher, From chemotherapy to biological therapy: A review of novel concepts to reduce the side effects of systemic cancer treatment (Review). *Inter. J. Oncol.* **54**, 407–419 (2019).
9. B. A. Chabner, T. G. Roberts Jr., Chemotherapy and the war on cancer. *Nat. Rev. Cancer* **5**, 65–72 (2005).
10. S. Senapati, A. K. Mahanta, S. Kumar, P. Maiti, Controlled drug delivery vehicles for cancer treatment and their performance. *Signal Transduct. Tar.* **3**, 7 (2018).
11. R. S. Riley, C. H. June, R. Langer, M. J. Mitchell, Delivery technologies for cancer immunotherapy. *Nat. Rev. Drug Discov.* **18**, 175–196 (2019).
12. M. Yang, O. T. Olaoba, C. Zhang, E. T. Kimchi, K. F. Staveley-O'Carroll, G. Li, Cancer immunotherapy and delivery system: An update. *Pharmaceutics* **14**, 1630 (2022).
13. L. Cai, J. Xu, Z. Yang, R. Tong, Z. Dong, C. Wang, K. W. Leong, Engineered biomaterials for cancer immunotherapy. *MedComm* **1**, 35–46 (2020).
14. J. Conde, N. Oliva, Y. Zhang, N. Artzi, Local triple-combination therapy results in tumour regression and prevents recurrence in a colon cancer model. *Nat. Mater.* **15**, 1128–1138 (2016).
15. A. Fakhari, J. A. Subramony, Engineered in-situ depot-forming hydrogels for intratumoral drug delivery. *J. Control. Release* **220**, 465–475 (2015).
16. S. B. Stephan, A. M. Taber, I. Jileaeva, E. P. Pegues, C. L. Sentman, M. T. Stephan, Biopolymer implants enhance the efficacy of adoptive T-cell therapy. *Nat. Biotechnol.* **33**, 97–101 (2015).
17. J. B. Wolinsky, Y. L. Colson, M. W. Grinstaff, Local drug delivery strategies for cancer treatment: Gels, nanoparticles, polymeric films, rods, and wafers. *J. Control. Release* **159**, 14–26 (2012).
18. B. D. Weinberg, E. Blanc, J. M. Ga, Polymer implants for intratumoral drug delivery and cancer therapy. *J. Pharm. Sci.* **97**, 1681–1702 (2008).
19. A. Hope, S. J. Wade, M. Aghmesheh, K. L. Vine, Localized delivery of immunotherapy via implantable scaffolds for breast cancer treatment. *J. Control. Release* **341**, 399–413 (2022).
20. M. Norouzi, B. Nazari, D. W. Miller, Injectable hydrogel-based drug delivery systems for local cancer therapy. *Drug Discov. Today* **21**, 1835–1849 (2016).
21. Y. H. Bae, K. Park, Targeted drug delivery to tumors: Myths, reality and possibility. *J. Control. Release* **153**, 198–205 (2011).
22. S. J. Yu, C. L. He, X. S. Chen, Injectable hydrogels as unique platforms for local chemotherapeutics-based combination antitumor therapy. *Macromol. Biosci.* **18**, 1800240 (2018).
23. Z. R. Lu, P. J. M. P. Qiao, Drug delivery in cancer therapy, quo vadis? *Mol. Pharm.* **15**, 3603–3616 (2018).
24. Z. X. Zhou, Z. R. Lu, Molecular imaging of the tumor microenvironment. *Adv. Drug Deliver. Rev.* **113**, 24–48 (2017).
25. D. F. Quail, J. A. Joyce, Microenvironmental regulation of tumor progression and metastasis. *Nat. Med.* **19**, 1423–1437 (2013).
26. N. U. Dharmaratne, A. R. Kaplan, P. M. Glazer, Targeting the hypoxic and acidic tumor microenvironment with pH-sensitive peptides. *Cell* **10**, 541 (2021).
27. Y. L. Dai, C. Xu, X. L. Sun, X. Y. Chen, Nanoparticle design strategies for enhanced anticancer therapy by exploiting the tumour microenvironment. *Chem. Soc. Rev.* **46**, 3830–3852 (2017).
28. J. J. Liu, Q. Chen, L. Z. Feng, Z. Liu, Nanomedicine for tumor microenvironment modulation and cancer treatment enhancement. *Nano Today* **21**, 55–73 (2018).
29. C. Zhang, D. Ni, Y. Liu, H. Yao, W. Bu, J. Shi, Magnesium silicide nanoparticles as a deoxygenation agent for cancer starvation therapy. *Nat. Nanotechnol.* **12**, 378–386 (2017).
30. Q. Chen, C. Wang, X. Zhang, G. Chen, Q. Hu, H. Li, J. Wang, D. Wen, Y. Zhang, Y. Lu, G. Yang, C. Jiang, J. Wang, G. Dotti, Z. Gu, In situ sprayed bioresponsive immunotherapeutic gel for post-surgical cancer treatment. *Nat. Nanotechnol.* **14**, 89–97 (2019).
31. A. L. Harris, Hypoxia-a key regulatory factor in tumour growth. *Nat. Rev. Cancer* **2**, 38–47 (2002).

32. P. Vaupel, A. Mayer, Hypoxia in cancer: Significance and impact on clinical outcome. *Cancer Metast. Rev.* **26**, 225–239 (2007).
33. A. Sundaram, L. Peng, L. Chai, Z. Xie, J. S. Ponraj, X. Wang, G. Wang, B. Zhang, G. Nie, N. Xie, M. R. Kumar, H. Zhang, Advanced nanomaterials for hypoxia tumor therapy: Challenges and solutions. *Nanoscale* **12**, 21497–21518 (2020).
34. X. S. Li, N. Kwon, T. Guo, Z. Liu, J. Yoon, Innovative strategies for hypoxic-tumor photodynamic therapy. *Angew. Chem. Int. Edit.* **57**, 11522–11531 (2018).
35. A. M. Shannon, D. J. Bouchier-Hayes, C. M. Condron, D. Toomey, Tumour hypoxia, chemotherapeutic resistance and hypoxia-related therapies. *Cancer Treat. Rev.* **29**, 297–307 (2003).
36. W. R. Wilson, M. P. Hay, Targeting hypoxia in cancer therapy. *Nat. Rev. Cancer* **11**, 393–410 (2011).
37. J. M. Brown, W. R. Wilson, Exploiting tumour hypoxia in cancer treatment. *Nat. Rev. Cancer* **4**, 437–447 (2004).
38. N. Baran, M. Konopleva, Molecular pathways: Hypoxia-activated prodrugs in cancer therapy. *Clin. Cancer Res.* **23**, 2382–2390 (2017).
39. S. C. Yang, Z. H. Tang, C. Y. Hu, D. W. Zhang, N. Shen, H. Y. Yu, X. S. Chen, Selectively potentiating hypoxia levels by combretastatin A4 nanomedicine: Toward highly enhanced hypoxia-activated prodrug tirapazamine therapy for metastatic tumors. *Adv. Mater.* **31**, 1805955 (2019).
40. S. B. Reddy, S. K. Williamson, Tirapazamine: A novel agent targeting hypoxic tumor cells. *Expert Opin. Inv. Drug.* **18**, 77–87 (2009).
41. L. Spiegelberg, R. Houben, R. Niemans, D. Ruysscher, A. Yaromina, J. Theys, C. P. Guise, J. B. Smaill, A. V. Patterson, P. Lambin, L. J. Duboisa, Hypoxia-activated prodrugs and (lack of) clinical progress: The need for hypoxia-based biomarker patient selection in phase III clinical trials. *Clin. Transl. Radiat. Oncol.* **15**, 62–69 (2019).
42. Y. Shao, B. Liu, Z. Di, G. Zhang, L. D. Sun, L. Li, C. H. Yan, Engineering of upconverted metal-organic frameworks for near-infrared light-triggered combinational photodynamic/chemo−/immunotherapy against hypoxic tumors. *J. Am. Chem. Soc.* **142**, 3939–3946 (2020).
43. C. Qian, P. Feng, J. Yu, Y. Chen, Q. Hu, W. Sun, X. Xiao, X. Hu, A. Bellotti, Q. D. Shen, Z. Gu, Anaerobe-inspired anticancer nanovesicles. *Angew. Chem. Int. Edit.* **56**, 2588–2593 (2017).
44. Q. Feng, Y. Li, X. Yang, W. Zhang, Y. Hao, H. Zhang, L. Hou, Z. Zhang, Hypoxia-specific therapeutic agents delivery nanotheranostics: A sequential strategy for ultrasound mediated on-demand tritherapies and imaging of cancer. *J. Control. Release* **275**, 192–200 (2018).
45. Y. Wang, Y. Liu, H. Wu, J. Zhang, Q. Tian, S. Yang, Functionalized holmium-doped hollow silica nanospheres for combined sonodynamic and hypoxia-activated therapy. *Adv. Funct. Mater.* **29**, 1805764 (2019).
46. Y. C. Su, I. Cockerill, Y. Wang, Y. X. Qin, L. Chang, Y. Zheng, D. Zhu, Zinc-based biomaterials for regeneration and therapy. *Trends Biotechnol.* **37**, 428–441 (2019).
47. Z. Shao, S. Cheng, Y. Zhang, H. Guo, X. Cui, Z. Sun, Y. Liu, Y. Wu, P. Cui, J. Fu, Q. Su, E. Xie, Wearable and fully biocompatible all-in-one structured "paper-like" zinc ion battery. *ACS appl. Mater. Inter.* **13**, 34349–34356 (2021).
48. N. A. de la Oliva, X. Navarro, J. del Valle, Time course study of long-term biocompatibility and foreign body reaction to intraneural polyimide-based implants. *J. Biomed. Mater. Res. A* **106**, 746–757 (2018).
49. C. P. Constantin, M. Aflori, R. F. Damian, R. D. Rusu, Biocompatibility of polyimides: A mini-review. *Materials* **12**, 3166 (2019).
50. X. L. Dong, L. Chen, J. Y. Liu, S. Haller, Y. G. Wang, X. Y. Xia, Environmentally-friendly aqueous Li (or Na)-ion battery with fast electrode kinetics and super-long life. *Sci. Adv.* **2**, 1501038 (2016).
51. Y. Lu, J. Chen, Prospects of organic electrode materials for practical lithium batteries. *Nat. Rev. Chem.* **4**, 127–142 (2020).
52. L. Yan, Y. Zhang, Z. Ni, Y. Zhang, J. Xu, T. Kong, J. Huang, W. Li, J. Ma, Y. Wang, Chemically self-charging aqueous zinc-organic battery. *J. Am. Chem. Soc.* **143**, 15369–15377 (2021).
53. F. Yue, Z. Tie, Y. Zhang, S. Bi, Y. Wang, Z. Niu, Proton chemistry induced long-cycle air self-charging aqueous batteries. *Angew. Chem. Int. Edit.* **61**, e2022085 (2022).
54. P. Poizot, J. Gaubicher, S. Renault, L. Dubois, Y. Liang, Y. Yao, Opportunities and challenges for organic electrodes in electrochemical energy storage. *Chem. Rev.* **120**, 6490–6557 (2020).
55. H. Peng, Q. Yu, S. Wang, J. Kim, A. E. Rowan, A. K. Nanjundan, Y. Yamauchi, J. Yu, Molecular design strategies for electrochemical behavior of aromatic carbonyl compounds in organic and aqueous electrolytes. *Adv. Sci.* **6**, 1900431 (2019).
56. J. Huang, X. Dong, Z. Guo, Y. Wang, Progress of organic electrodes in aqueous electrolyte for energy storage and conversion. *Angew. Chem. Int. Edit.* **59**, 18322–18333 (2020).
57. Y. T. Li, J. M. Liu, Z. C. Wang, J. Jin, Y. L. Liu, C. Y. Chen, Z. Y. Tang, Optimizing energy transfer in nanostructures enables in vivo cancer lesion tracking via near-infrared excited hypoxia imaging. *Adv. Mater.* **32**, 1907718 (2020).
58. M. Oginuma, Y. Harima, O. A. Tarazona, M. Diaz-Cuadros, A. Michaut, T. Ishitani, F. Z. Xiong, O. Pourquié, Intracellular pH controls WNT downstream of glycolysis in amniote embryos. *Nature* **584**, 98–101 (2020).
59. Z. Z. Zou, H. C. Chang, H. L. Li, S. M. Wang, Induction of reactive oxygen species: An emerging approach for cancer therapy. *Apoptosis* **22**, 1321–1335 (2017).
60. B. W. Yang, Y. Chen, J. L. Shi, Reactive oxygen species (ROS)-based nanomedicine. *Chem. Rev.* **119**, 4881–4985 (2019).
61. C. Gorrini, I. S. Harris, T. W. Mak, Modulation of oxidative stress as an anticancer strategy. *Nat. Rev. Drug Discov.* **12**, 931–947 (2013).

Acknowledgments

Funding: This work was supported by National Natural Science Foundation of China (nos. 21935003, 22104017, 22179119, 22088101, 21725502, and 51961145403). **Author contributions:** J.H. and Y.X. conceived this idea. J.H., P.Y., F.Z., Y.W., and Y.X. designed the experiments. J.H., X.D., and J.X. performed the material preparation and characterization. P.Y. and J.M. performed the bioexperiments and data analysis. J.H., M.L., and D.B. carried out the electrochemical measurements and data analysis. J.H., P.Y., and F.Z. co-wrote the paper. **Competing interests:** The authors declare that they have no competing interests. **Data and materials availability:** All data needed to evaluate the conclusions in the paper are present in the paper and/or the Supplementary Materials.

Submitted 20 October 2022
Accepted 27 February 2023
Published 31 March 2023
10.1126/sciadv.adf3992